MgFe$_2$O$_4$/CNTs nanocomposite: Synthesis, Characterization, and Photocatalytic Activity

Ibrahim F. Waheed[1], Omer Yasin Thayee Aljanabi[2*], Abdalghany K. Ibrahim[1], Peter J. S. Foot[3], Muayad A.S. Alkarawi[2], Baidaa M. Ali[1], Faiz M. Al-Abady[1]

[1]College of Science, Dept. of Industrial Chemistry, Tikrit University (Tikrit, Iraq)

[2]College of Petroleum Processes Engineering, Petroleum & Gas Refining Engineering, Tikrit University (Tikrit, Iraq)

[3]Kingston University London, School of Chemical and Pharmaceutical Sciences, Kingston upon Thames KT1 2EE (UK)

* Corresponding author: omaroilgas@tu.edu.iq

Abstract

Magnesium ferrite is a visible light absorber, and when combined with multiwall carbon nanotubes (MWCNTs), it can lead to low electron-hole recombination rates, thus improving its photocatalytic activity. In this work, a novel MgFe$_2$O$_4$/CNTs nanocomposite catalyst has been synthesized via anchoring MgFe$_2$O$_4$ nanoparticles onto MWCNTs surface by a sol-gel and microwave-assisted route. The prepared catalyst was characterized by X-ray diffraction, Fourier-transform infrared spectroscopy, scanning and transmission electron microscopy, energy-dispersive x-ray analysis and vibrating scanning magnetometry. MgFe$_2$O$_4$ nanoparticles showed a cubic inverse spinel ferrite structure, while MgFe$_2$O$_4$/CNTs nanohybrids showed combinations of both structures. Morphology studies including Brunauer-Emmett-Teller (BET) analysis confirmed a 40 m^{2}g^{-1} specific surface area with narrow mesoporous size distribution for the MgFe$_2$O$_4$/CNTs nanocomposite. The photocatalytic performance of the new catalyst was assessed by photodegradation of methylene blue (MB). The experimental results demonstrated that MgFe$_2$O$_4$/CNTs exhibited strong photocatalytic activity, catalysing the photooxidation of about 98% of MB in 25 minutes under sunlight.

Key words: MgFe$_2$O$_4$/CNTs; Magnetic properties; Photocatalysis; MB degradation.

1. Introduction

Nowadays, water pollution caused by synthetic dyes has become one of the challenges that the world faces as an outstanding environmental problem, posing serious threats to living organisms [1-3]. Several techniques such as adsorption by activated carbon, ultrafiltration

membranes, piezocatalysis and photocatalytic degradation have been extensively employed to eliminate water pollution [4-8]. However, besides their ineffectiveness in raw water treatment, these purification technologies have encountered multiple economic restrictions like the need for complicated instruments, high capital requirements, high energy consumption, and operational costs [9,10]. Nonetheless, photocatalysis has found much interest among water purification agencies due to its powerful, environmentally-friendly action [11].

Photocatalytic degradation is based on semiconductors that can be excited to an energy level higher than their band gap, inducing the formation of energy-rich electron-hole pairs, which can be involved in redox reactions resulting in the decomposition of synthetic dyes [12-14]. The efficiency of such processes is strongly related to the transport of the photogenerated carriers (electrons and holes) which in turn depends on the materials' morphology, particle size, size distribution, their dose, pollutant concentration and pH [15,16]. Among a variety of photocatalysts, semiconductors with spinel structures such as the ferrites family $ZnFe_2O_4$, $MgFe_2O_4$, and $CoFe_2O_4$ etc. have received enormous interest in the field of water splitting and removing contaminants because of their low cost, unusual band structures and the environmental benignity of their constituent elements [17-20].

Natural ferrites have magnetic properties and high electrical resistivity, which makes them compatible with many types of modern electronic devices [21,22]. The spinel ferrite structures have the general chemical formula MFe_2O_4, where M is Mn^{2+}, Co^{2+}, Ba^{2+}, Zn^{2+}, Cd^{2+}, Ni^{2+}, Mg^{2+}, Cu^{2+}, etc. The structure of a spinel is determined by the bonding and arrangement of the oxygen ions (O^{2-}) within the lattice. The unit cell of a spinel lattice contains eight formula units $[AB_2O_4]$ in which the large oxygen anions (32 from O^{-2}) form a close-packed face-centered cubic FCC structure. The few metal cations occupy interstitial sites: tetrahedral (8) or (A) and octahedral (16) or (B) sites, so the resulting local symmetries of these sites are different [23-25]. Among the diverse range of spinel ferrites, magnesium ferrite $MgFe_2O_4$ abbreviated MFO is a bi-oxide with inverse spinel structure and is a soft magnetic n-type semiconductor. MFO semiconductor is a promising UV-visible absorber due to its narrow band gap and its magnetic nature which helps its separation from aqueous systems [26-29]. Furthermore, MFO has good photostability in alkaline or acidic solutions, rendering it a good candidate for environmental remediation by utilizing active surface species (H^+, $^.OH$ and $^.O^{2-}$), especially in photocatalytic degradation processes. Nonetheless, the fast recombination of charge-carriers in pure $MgFe_2O_4$ results in reduced photocatalytic efficiency under visible light [29,31]. To diminish this problem, MFO photocatalysts have

often been used as nanocomposites with other compounds for photodegradation of different water pollutants [32]. Such materials are $Mg_{1-x}Zn_xFe_2O_4$ nanocomposite for degradation of MB [16] and $MgFe_2O_4/TiO_2$ for degradation of Rhodamine B [33], $MgFe_2O_4$-GO nanocomposite for degradation of MB under visible light irradiation [34]. Concomitantly, multi-walled carbon nanotubes (CNTs) were combined with various compounds to improve photocatalytic activity [35,36].

Carbon nanotubes (CNTs) have received great attention in the area of supported heterogeneous catalysis owing to their remarkable features such as large specific surface area, good chemical stability and excellent conductivity [37-39]. Based on these properties, combining CNTs and magnetic materials to form a binary composite catalyst helps encourage charge carrier separation and photocatalytic activity. Despite the many studies and applications based on CNTs composites, to the best of our knowledge there is no detailed study of the structural, magnetic and surface area properties of $MgFe_2O_4/CNTs$ nanocomposites to date. For that reason, we were motivated to work on MFO/CNTs $MgFe_2O_4/CNT$ nanocomposites as photocatalysts to be used in water purification technology. Our novel catalyst supported CNTs were synthesized by microwave-assisted route and characterized by XRD, FTIR spectroscopy. Surface investigations were performed by scanning electron microscopy (SEM) in conjunction with energy dispersive X-ray analysis (EDX), transmission electron microscopy (TEM), and N_2 adsorption-desorption isotherms. The photocatalytic activity of our $MgFe_2O_4/CNTs$ nanocomposite was evaluated through the photodegradation reaction of methylene blue (MB) in aqueous solution. The results showed that the $MgFe_2O_4/CNT$ catalyst exhibited a high level of activity for the photodegradation under sunlight.

2. Experimental

2.1. Materials

All chemicals used for the catalyst preparation were of analytical grade with 99% purity and were used as-received without further purification. Deionized water was used for the synthesis of $MgFe_2O_4/CNT$ nanocomposites was Milli-Q water (resistivity greater than 18.2 MΩ.cm). Magnesium nitrate $Mg(NO_3)_2.6H_2O$ and iron (III) nitrate $Fe(NO_3)_3.9H_2O$ were purchased from S.d. Fine-Chem Limited Mumbai. Poly(vinylpyrrolidone) K30 (PVP) (MW= 40000) was purchased from DIREVO Industrial Biotechnology Germany. Multi-walled carbon nanotubes (MWCNTs) (purity >95%, diameter 10–20 nm) were purchased from Chengdu Organic Chemical Co. Ltd China.

2.2. Synthesis of MgFe$_2$O$_4$ nanoparticles

Nanocrystalline magnesium ferrite (MgFe$_2$O$_4$) was synthesized via the auto combustion technique, following a procedure published elsewhere [27]. The molar ratio of combustion fuel to metal ions (F:M) was 1:2, while the molar ratio of Mg:Fe was 1:2. In a typical synthesis, an amount of nitrate precursors i.e. Mg(NO$_3$)$_2$.6H$_2$O and Fe(NO$_3$)$_3$.9H$_2$O were dissolved in the minimum amount of deionized water. Dissolved nitrates were then mixed for a while, followed by adding combustion fuel (PVP) to initiate the exothermic reaction. The pH value of the solution mixture was adjusted to 8 with ammonia solution to ensure homogenization of the added PVP with the nitrates mixture. The reaction mixture was mixed using magnetic stirring for an additional 10 min at room temperature and heated gently to about 90°C with constant stirring until a gel was obtained. The formed sol-gel product was transferred to a vacuum oven and kept at 150°C to obtain a dry gel. A loose and very fine magnesium ferrite powder was produced after the dried gel had spontaneously combusted in air. The final burnt powder was thermally annealed at 950°C in ambient atmosphere to obtain well-crystallized MgFe$_2$O$_4$ nanoparticles.

2.3. Synthesis of MgFe$_2$O$_4$/CNTs nanocomposite catalyst

Initially, the pristine MWCNTs were pretreated by mixing with an acid so that increases their hydrophilicity by creating oxygenated functional groups on the nanotube surface. Following a certain methodology [27], 0.4 g of MWCNTs were dispersed in a solution consisting of 60 mL HNO$_3$ (~65% wt.) and 10 mL H$_2$SO$_4$ (~98% wt.). The mixture was transferred into a fully-equipped reactor vessel and refluxed at 120°C for 10 h. The acid-treated MWCNTs were filtered and washed several times with deionized water until the pH value reached 7. The treated nanotubes were dried overnight at 100°C in an oven and ground to powder. For the synthesis of the MgFe$_2$O$_4$/CNTs nanocomposite, 0.3 g of treated CNTs was introduced into 50 mL of deionized water and completely dispersed by sonication for 30 min using a bath sonicator device, Branson 2510. 0.5 g of the presynthesized MgFe$_2$O$_4$ powder was dispersed in 50 mL of deionized water and sonicated for 30 min. Then the two solutions were mixed and 10 mL of hydrazine hydrate was added to the mixed solutions, followed by sonication for 1.5 h at 35°C. The resulting mixture was transferred into a microwave oven (Emerson MW8119SB) for 10 min. The solid product was separated and washed repeatedly with absolute ethanol and deionized water to remove impurities, and the MgFe$_2$O$_4$/CNTs nanocomposite was obtained after drying at room temperature under vacuum. A schematic

representation of the steps involved during the synthesis of $MgFe_2O_4$/CNTs nanocomposites is given in Fig.1.

Fig. 1. Schematic diagram of the synthesis of $MgFe_2O_4$/CNTs nanocomposites using the microwave-assisted route and its application for MB photodegradation.
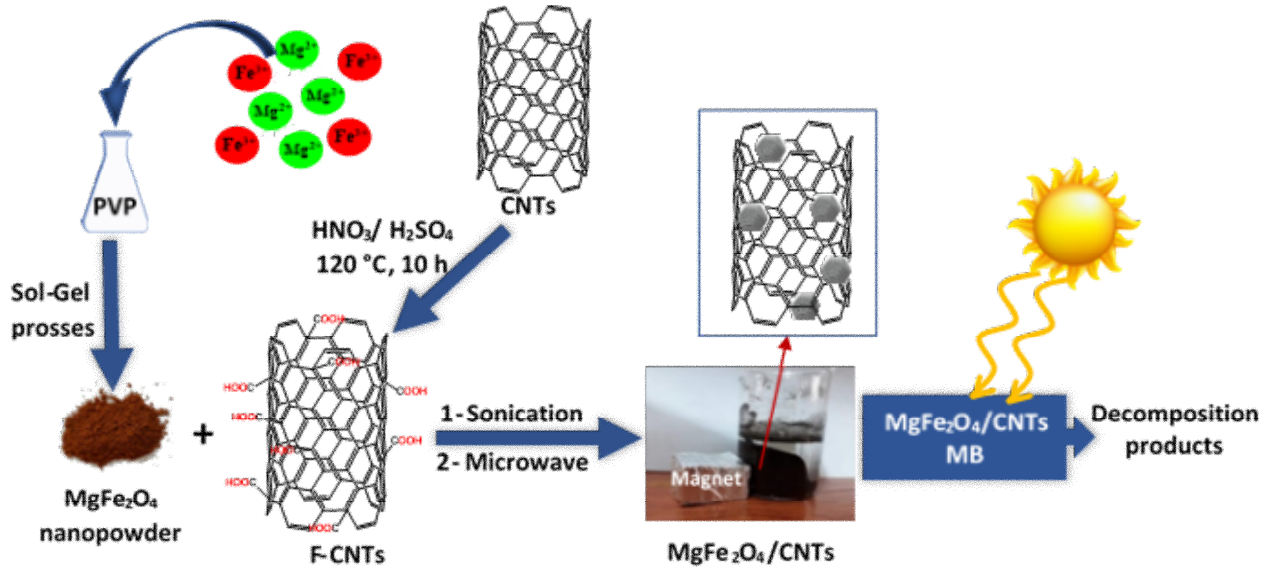
2.4. Materials characterization

The crystalline structures of the synthesized materials were characterized by XRD using a Rigaku Miniflex with Cu Kα wavelength radiation (λ= 1.5406Å). The mean dimension (D_{XRD}) of crystalline coherent domains (i.e., "crystallite size") was calculated using the Scherrer equation [40]:

$$D_1 XRD = K (/ (\beta \, cos\theta) \qquad (1)$$

where K is a constant related to the crystallite shape ($K = 0.9$), θ is the Bragg angle and β is the contribution of the crystallite size to the full width at half maximum (FWHM) of the diffraction peak correspondent in radians.

The lattice constant a is calculated from the following relation [41]:

$$a = d_{hkl}\sqrt{h^2 + k^2 + l^2} \qquad (2)$$

where d the interplanar distance for the plane hkl. The X-ray density (Dx) was calculated using the following formula [42]:

$$Crystallinity\,\% = \frac{Diffraction\ peak\ intensity}{Total\ intensity} \times 100 \qquad (3)$$

The crystalline phase was identified using the International Centre for Diffraction Data (ICDD) database. N_2 adsorption-desorption measurements were carried out to measure the specific surface areas of the samples, according to the Brunauer-Emmett-Teller (BET)

method, and pore volumes with the Barret-Joyner-Halenda (BJH) model. The surface morphology of the obtained nanocomposites was inspected by field emission scanning electron microscopy (FE-SEM) (Model: ZEISS Sigma 300) and transmission electron microscopy (TEM). Observations were carried out using a JEOL, JEM-2100F system at an operating voltage of 200 kV. For the TEM measurements, a small amount of sample was dispersed in ethanol using an ultrasonic bath for 10 min. A drop of the sonicated sample solution was released on the top surface of a carbon film supported copper grid then allowed to dry in the air before analysis. Sample composition was confirmed by energy dispersive X-ray spectroscopy (EDX) (ZEISS Sigma 300). The Fourier-transform infrared spectra (FTIR) of magnesium ferrite powders (as pellets in KBr) were recorded with an IR Shimadzu 8400 spectrophotometer over the range of (400-4000) cm^{-1}. The optical properties were analyzed using Diffuse Reflectance Spectroscopy (Uv-vis-DRS) JASCO-V650 with an integrating sphere (ILV-724) (λ= 300-800 nm). The magnetization measurements were performed using a vibrating scanning magnetometer (VSM) (Cryogenic Limited PPMS) under an applied field of ±1 T at room temperature. The electron spin resonance (ESR) spectroscopy experiments were carried out on a Bruker ER200-SRC, spectrometer; samples were produced via mixing 0.05 g of the as-prepared MgFe$_2$O$_4$/CNTs in a 25mM 5,5′-dimethyl-1-pyrroline-N-oxide (DMPO) solution.Measurements were carried out on a 50 mL aqueous dispersion for DMPO-$^{\bullet}$OH and a 50 mL alcohol dispersion for DMPO-$^{\bullet}$O$_2^-$ under simulated solar light irradiation.

2.5. Photocatalytic activity test

The photocatalytic activity of our MgFe$_2$O$_4$/CNTs nanocomposite catalyst was measured by utilizing the photodegradation reaction of methylene blue under solar irradiation. For each run, 0.03 g of photocatalyst was dispersed in 50 mL of a 10 mg L^{-1} methylene blue aqueous solution. Before the photocatalytic test, the mixture (i.e. photocatalyst and MB) was stirred in the dark for 30 min to achieve adsorption equilibrium between MB, photocatalyst and water. Then, the photodegradation reaction proceeded by irradiating the solution for 25 min under visible light. 5 mL of suspension was withdrawn after every 5 min from the solution during the photocatalytic process. All the experiments were done under direct sunlight (100,000±100 lux) during fixed periods of sunlight and in the natural environment without stirring. The collected samples were immediately filtered and then centrifuged to separate the nanocomposite from the dye solution. The samples were analyzed using a Uv-vis spectrophotometer at λ_{max} = 664nm to obtain the concentration of methylene blue after the elapsed time interval (C_t). Dye degradation with time was evaluated using the following equation:

$$\%Degradation = \frac{(C_0 - C_t)}{C_0} \times 100 \qquad (4)$$

where C_0 is the initial concentration of the dye and C_t the concentration at a given reaction time.

3. Results and Discussion

3.1. XRD and FTIR measurements

(Fig. 2-left) shows the XRD patterns of $MgFe_2O_4$/CNTs and pristine $MgFe_2O_4$ nanoparticles after calcination at 900°C for 3 h. As can be seen, the $MgFe_2O_4$ nanoparticles exhibited characteristic diffraction peaks of (111), (220), (311), (222), (400), (331), (422), (511), (440), (531), (620), and (533) crystal planes at 2θ values of 18.3°, 30.1°, 35.5°, 37.1°, 43.1°,49.5°, 53.4°, 57.0°, 62.6°, 64.0°, 70.9°, and 74.0°, respectively. These data can be indexed as a face-centered cubic phase (space group *Fd3m*) of spinel magnesium ferrite (ICSD card no. 01-071-1232) with no peaks related to Mg and Fe oxides. A strong and sharp diffraction peak (002) located at 26.6° in the XRD patterns of $MgFe_2O_4$/CNTs nanocomposite belonged to the CNTs [43]. Moreover, a significant reduction in the diffraction peak intensities of the $MgFe_2O_4$ nanoparticles after anchoring onto MWCNTs was observed. The average crystallite size (D_{XRD}) for $MgFe_2O_4$ nanoparticles and $MgFe_2O_4$/CNTs nanocomposite was 39.0 and 43.2, respectively. Furthermore, the XRD pattern showed that the unit cell parameter of the $MgFe_2O_4$ nanoparticles (*a*= 8.381 nm) was smaller than $MgFe_2O_4$ with CNTs (*a*= 8.387 nm). Experimental and calculated data obtained from XRD patterns of the studied materials are summarized in Table 1.

Table 1. Summary of various physical parameters of $MgFe_2O_4$ nanoparticles and $MgFe_2O_4$/CNTs nanocomposite.

Parameters	Units	Pristine $MgFe_2O_4$	$MgFe_2O_4$/CNTs
Crystallite size (D_{SEM})	nm	35.16	50.0
Crystallite size (D_{TEM})	nm	35.5±5	50
Crystallite size (D_{XRD})	nm	39.0	43.2
Lattice constant (*a*)	Å	8.381	8.387
Unit cell volume (V)	Å^3	588.6	589.9
Crystallinity (%)	-	77.5%	45.6%
Specific surface area (SA_{BET})	$m^2.g^{-1}$	4.6261	40.051
Total pore volume, (V_{total})	$cm^3.g^{-1}$	0.034992	0.3029
Mean pore diameter	nm	30.256	30.247
Saturation magnetization, (M_S)	emu. g^{-1}	24.08	17.59
Remanence (M_R)	emu. g^{-1}	8.43	4.44
Coercive field (H_C)	Oe	79.38	58.13

Fig. 2. (left): XRD patterns of $MgFe_2O_4$ and $MgFe_2O_4$/CNTs; **(right):** FTIR spectrum of $MgFe_2O_4$/CNTs (a) and $MgFe_2O_4$ nanoparticles calcined at 900°C (b).
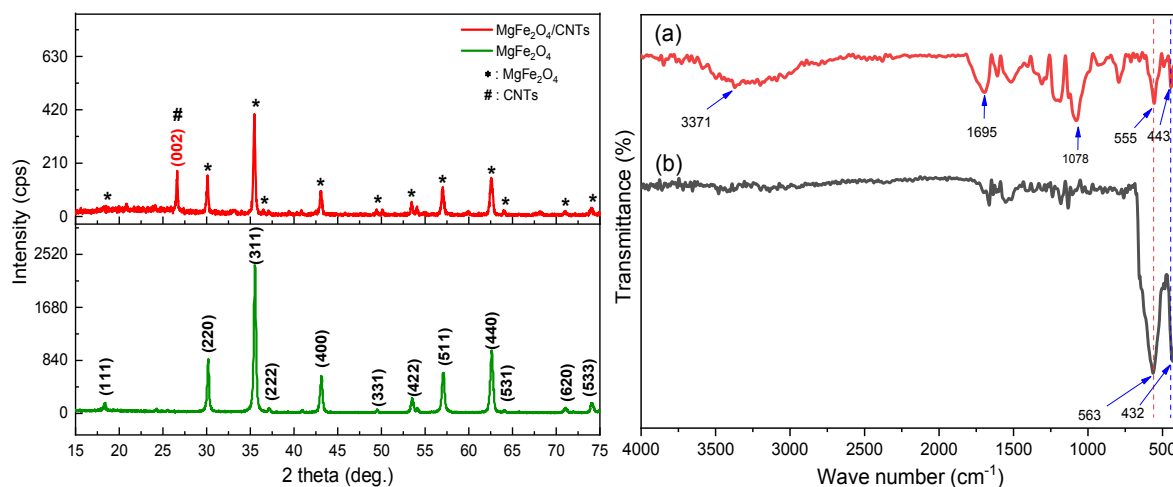
The FTIR spectra of the $MgFe_2O_4$ nanoparticle and $MgFe_2O_4$/CNTs nanocomposite in the range 400 to 4000 cm^{-1} are shown in Fig. 2-right. The FTIR spectrum of $MgFe_2O_4$ NPs showed two remarkable absorption bands at 563 and 432 cm^{-1} attributed to the ionic bonds (Fe-O and Mg-O) which are indicative of the formation of $MgFe_2O_4$ [44]. In the case of the $MgFe_2O_4$/CNTs nanocomposite, the FTIR peaks at 3371 cm^{-1} (O-H bond), 1695 cm^{-1} (C=O bond), 1515 cm^{-1} (C=C bond), 1309 cm^{-1} (O-H bond), 1078 cm^{-1} (C-O bond) were observed. This suggests that the surface of CNTs possesses some oxygen-containing functional groups which enhance physical interaction between $MgFe_2O_4$ and MWCNTs. Other evidence that physical interaction between $MgFe_2O_4$ and MWCNTs had taken place is that the peaks of the pristine $MgFe_2O_4$ NPs were shifted from 563 to 555 cm^{-1} and from 432 to 443 cm^{-1} in the MFO/CNTs.

3.2. Morphology and N_2 adsorption measurements

The morphology and surface structure of the studied nanomaterials were examined by SEM/EDX and TEM techniques. Fig. 3 a-c depicts SEM micrographs and their respective energy dispersive X-ray patterns (EDX) of pristine $MgFe_2O_4$ nanoparticles and $MgFe_2O_4$/CNTs nanocomposite. The observations for the pristine $MgFe_2O_4$ nanoparticles Fig. 3a demonstrates a polyhedric and spherical morphology with some aggregations forming a larger particles. These aggregations, however, caused a reduction in the surface area of our photocatalyst. The MFO aggregations were also increased upon addition of CNTs, which may be attributed to the preparation methodology (Fig. 3c). However, some of $MgFe_2O_4$ nanoparticles were partly naked with a relatively low density of CNTs. The elemental composition of the synthesized samples was determined by EDX analysis. The EDX

spectrum for the pristine MFO Fig. 3b indicates the presence of Mg, Fe and O in the sample, with an atomic ratio of Mg to Fe of about 1:2, whereas, for the MFO/CNTs, the EDX pattern Fig. 3d shows C, Mg, Fe and O peaks related to the $MgFe_2O_4$ nanoparticles in the MWCNT. The qualitative analysis of C, Mg, Fe and O in the $MgFe_2O_4$/CNTs nanocomposite as determined by EDX analysis is shown in the inset of Fig. 3d.

Fig. 3. SEM microphotographs of (a) pristine $MgFe_2O_4$ NPs; (c) $MgFe_2O_4$/CNTs nanocomposite; and their EDX patterns (b) pristine $MgFe_2O_4$ NPs; (d) $MgFe_2O_4$/CNTs nanocomposite.
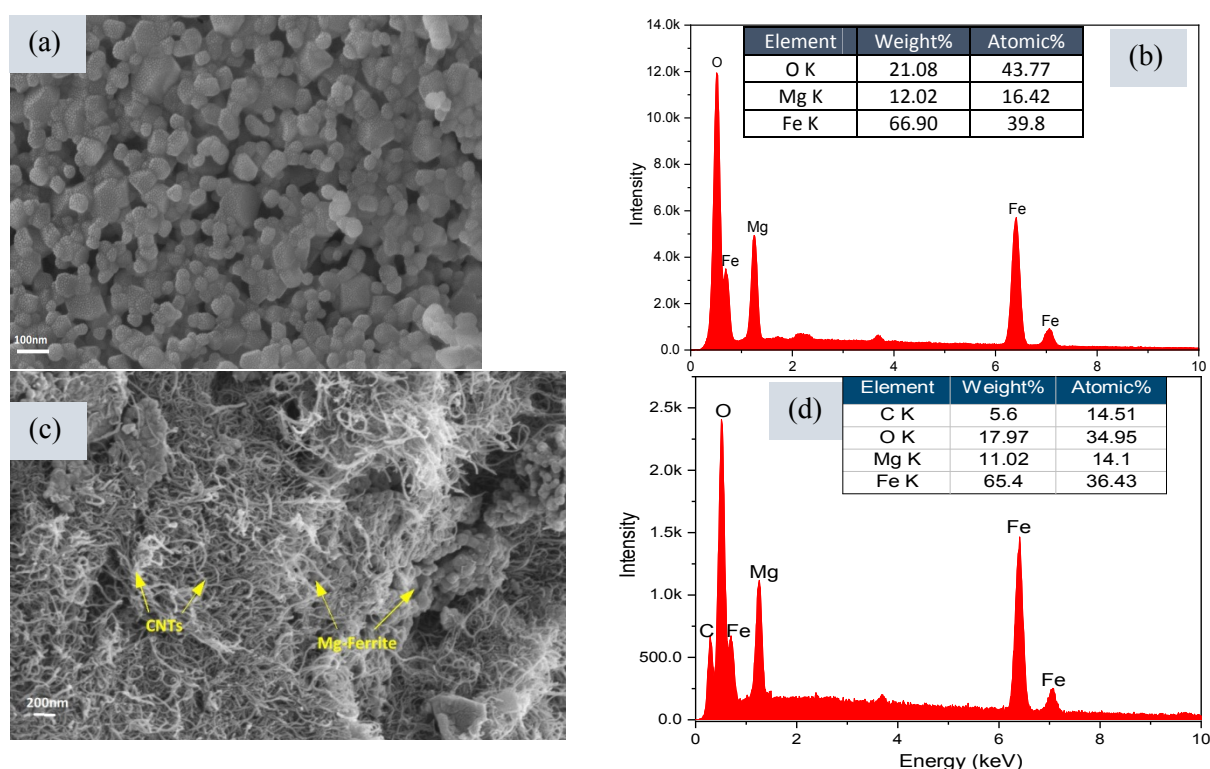
The detailed morphology and crystalline structure of the $MgFe_2O_4$ NPs and $MgFe_2O_4$/CNTs nanocomposite were studied by TEM; the corresponding FFT patterns as well as diameter histograms of these two samples are shown in Fig. 4 a-j. Fig. 4a and Fig. 4e reveal the TEM images and diameter histogram for $MgFe_2O_4$ nanoparticles, respectively. The latter histogram displays a homogenous crystallite size distribution in the range 35.5±5 nm. Figs. 4f and 4g are TEM images of $MgFe_2O_4$/CNTs nanocomposite, which reveal that very small $MgFe_2O_4$ nanoparticles were anchored onto the external surface of MWCNTs. The partial coating of MWCNTs by $MgFe_2O_4$ nanoparticles increases access to the catalytic sites and thus leads to an increase in photocatalytic activity [45]. The CNTs reveal a multi-wall structure and an average diameter of about 12.5 nm. Moreover, CNTs with good graphitic structure will exhibit good electronic properties, which are crucial for $MgFe_2O_4$/CNTs photocatalytic

activity. In addition, the HR-TEM image was used to determine the lattice spacing of pristine $MgFe_2O_4$ and $MgFe_2O_4$ nanoparticles in $MgFe_2O_4$/CNTs nanocomposite (Fig. 4c and Fig. 4i).

Fig. 4. TEM analysis of $MgFe_2O_4$ NPs and $MgFe_2O_4$/CNTs nanocomposite: (a) (b) (c) and (d) HR-TEM image shows the lattice spacing of $MgFe_2O_4$ NPs with the corresponding FFT pattern of $MgFe_2O_4$; (e) The particles diameter distribution of $MgFe_2O_4$ NPs; (f) and (g) TEM images of $MgFe_2O_4$/CNTs nanocomposite; (h) The diameter distribution of CNTs; (i) and (j) HR-TEM image with the corresponding FFT pattern of $MgFe_2O_4$/CNTs nanocomposite.
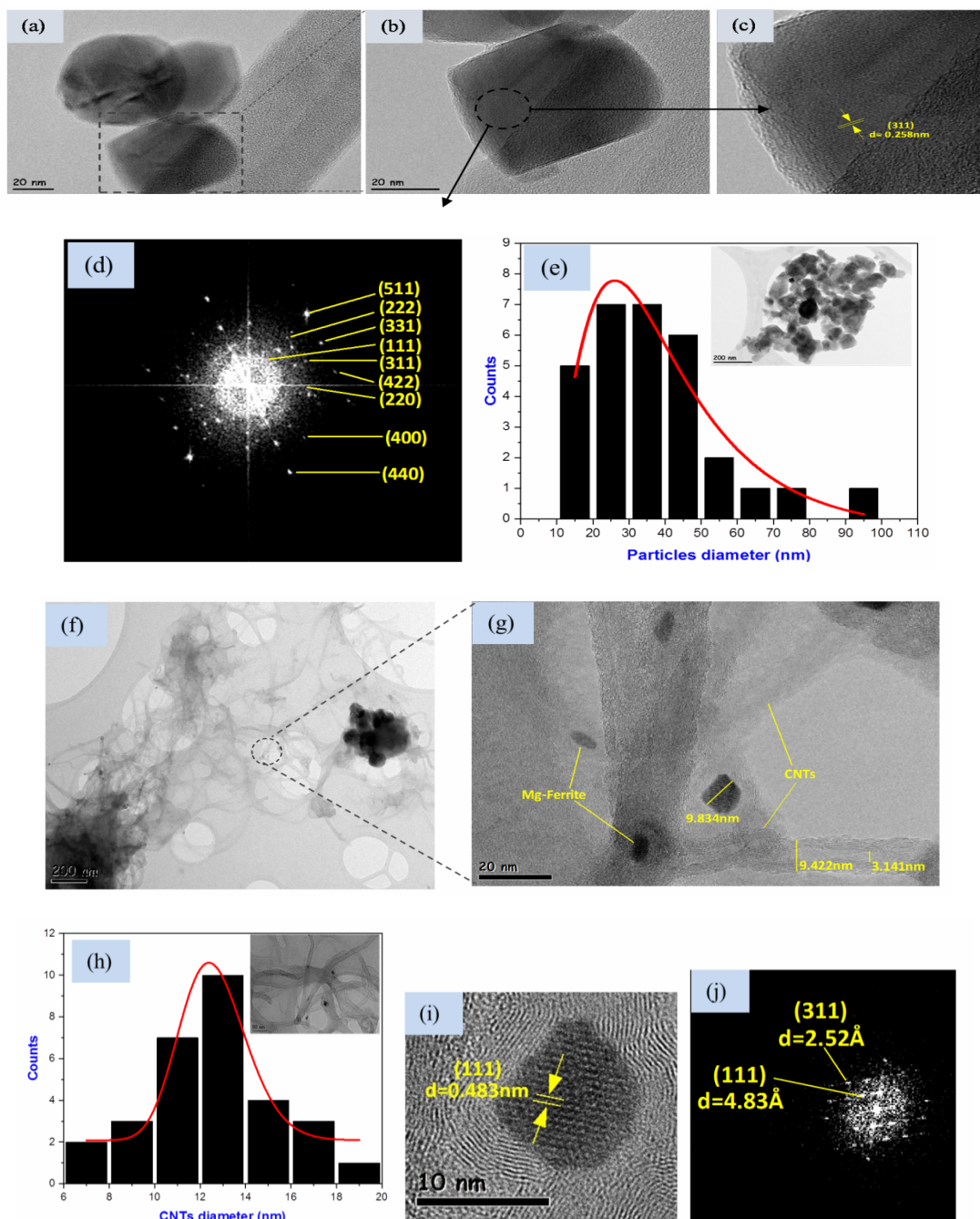
The size of $MgFe_2O_4$ nanoparticles anchored on MWCNTs surface was found to be 10 nm and the d-spacing was 0.483 nm for the (111) planes. The corresponding FFT patterns of both samples showed spotty ring patterns without any additional diffraction spots, revealing their crystalline spinel structure. The interplanar spacings (d_{hkl}) from the FFT patterns illustrated in Figs. 4d and 4j were in good agreement with standard data (ICSD: 01-071-1232). The diffraction rings are attributable to the (111), (220), (311), (400), (422), (511), and (440) planes. This result confirmed the crystalline structure of $MgFe_2O_4$ NPs indicated by XRD.

The N_2 adsorption-desorption isotherms of the porous pristine $MgFe_2O_4$ NPs and $MgFe_2O_4$/CNTs nanocomposite are shown in Fig. 5a-d. The studied samples exhibited type IV isotherm H_3 hysteresis loops. The emergence of such hysteresis loops is attributed to irreversible desorption, which mainly indicates that the materials had mesoporous structures. Remarkably, the isotherm loops of $MgFe_2O_4$ NPs and $MgFe_2O_4$/CNTs nanocomposite displayed a narrow hysteresis loop at relatively high pressures between 0.30-0.98 and 0.64-0.98, respectively, which is another evidence for the mesoporosity that is suitable for catalysis. As seen in Fig. 5a and Fig. 5c, the evaluation of nitrogen sorption data revealed that $MgFe_2O_4$/CNTs nanocomposite had a significantly higher BET specific surface area (SA_{BET}) (40.051 m^2g^{-1}) than the pristine $MgFe_2O_4$ nanoparticles (4.626 m^2g^{-1}). The high surface area and mesoporous structure of the $MgFe_2O_4$/CNTs may be due to two reasons: firstly, during the sol-gel process, the reaction of $MgFe_2O_4$ released gases which in turn formed mesoporous structures, and the second reason is the small diameter of MWCNTs which is around 6-20nm (Fig. 4h).

The pore size distribution of pristine $MgFe_2O_4$ (Fig. 4b) shows long-range mesoporous domains extending from 1.2 to 95 nm, with an effective pore size of approximately 1.2 nm. This suggests the existence of disordered porous structures in the pristine $MgFe_2O_4$. On the other hand, $MgFe_2O_4$/CNTs exhibits mesoporous domains in a narrower range with effective pore size around 14 nm (Fig. 4d). This suggests the presence of ordered porous structures in the $MgFe_2O_4$/CNTs. According to the International Union of Pure and Applied Chemistry (IUPAC), the size of 14 nm classifies our nanocatalyst as a mesoporous catalyst. Moreover, this value excellently agrees with the results obtained from the hysteresis loops in Fig. 5c. Such well-developed pore size distributions are of great importance for photocatalytic applications, since they could assist the reactants to reach the catalytic surfaces more easily[46, 47]. The specific surface area (SA_{BET}), total pore volume and average pore size of all the synthesized samples, obtained from the isotherms, are transcribed in Table 1.

Fig. 5. N$_2$ adsorption-desorption isotherms: (a) pristine MgFe$_2$O$_4$ nanoparticles; (c) MgFe$_2$O$_4$/CNTs nanocomposite; (b) BET surface area: pore size distribution plots of pristine MgFe$_2$O$_4$ nanoparticles; (d) BET surface area: pore size distribution plots of MgFe$_2$O$_4$/CNTs nanocomposite.
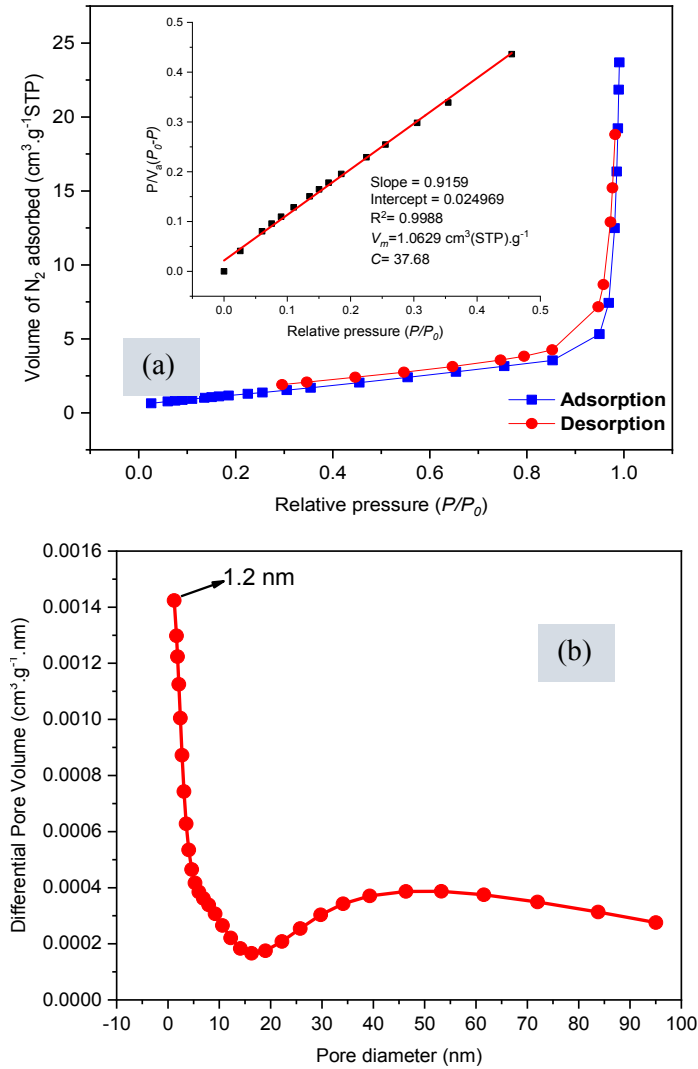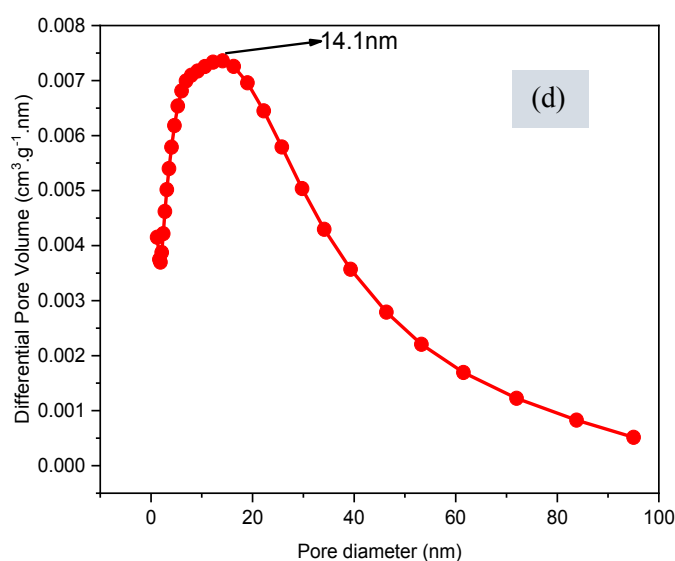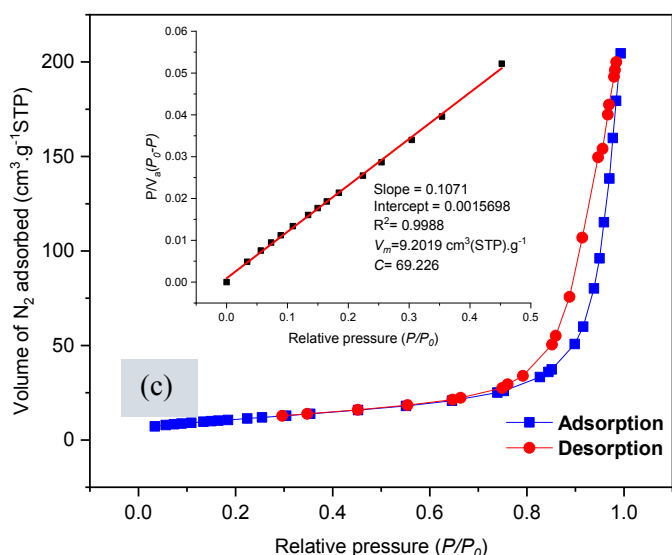
3.3. Magnetic studies

The magnetic hysteresis loops of pristine $MgFe_2O_4$ nanoparticles and $MgFe_2O_4$/CNTs nanocomposite are shown in Fig. 6. The magnetic parameters collected from vibrational sample magnetometer (VSM) at room temperature are summarized in Table 1. The magnetic hysteresis graph shows that the samples have soft superparamagnetic behavior. However, from the graph, the saturation magnetization (Ms) value for $MgFe_2O_4$ nanoparticles was 24.08 emu/g, while it was 17.59 emu/g for $MgFe_2O_4$/CNTs nanocomposite. This decline in the saturation magnetization might be attributed to the diamagnetic property of MWCNTs in the nanocomposites [48] and/or to the presence of a magnetically dead or antiferromagnetic layer on the nanocomposite surface [49]. Nonetheless, $MgFe_2O_4$/CNTs still have a high saturation magnetization that enhances its recovery from water after being exposed to an external magnetic field. This magnetic feature provides a distinct advantage over conventional photocatalysts due to the ready recoverability and recyclability of the suspended

13

system [50]. On the other hand, the decrease in the coercive field (H_C) value of MgFe$_2$O$_4$/CNTs nanocomposite is a sign of the formation of a soft ferrite material. Furthermore, the change in the coercivity values in MWCNTs is of interest in terms of magnetic crystalline anisotropy [51].

Fig. 6. Magnetic hysteresis curves of MgFe$_2$O$_4$ and MgFe$_2$O$_4$/CNTs at room temperature.
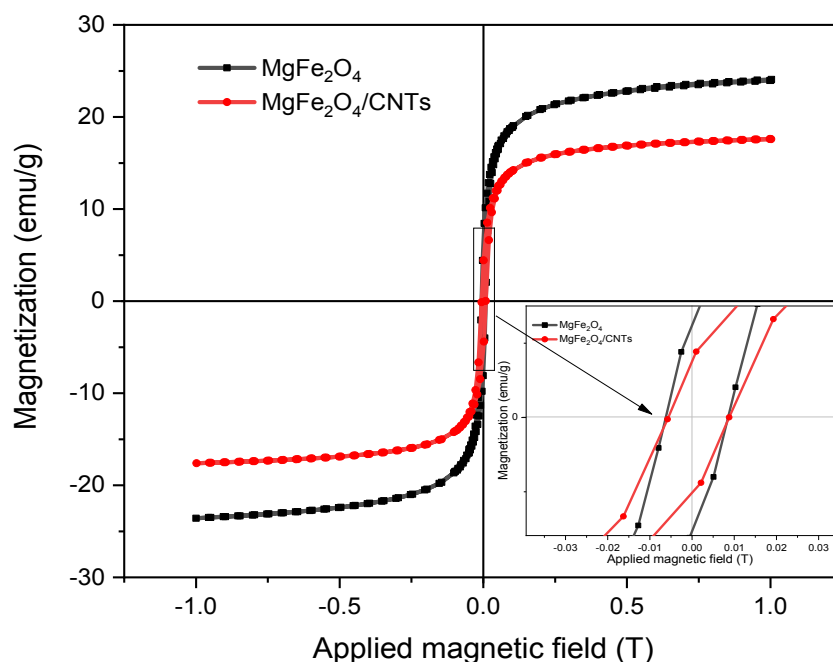
3.4. UV-visible spectroscopy

The optical properties of as-prepared MgFe$_2$O$_4$ NPs and MgFe$_2$O$_4$/CNTs nanocomposite were recorded using UV-vis DRS spectroscopy. The graphical results in Fig. 7 (left), reveal that both samples displayed a broad absorption band in the range (250-800 nm). However, the MgFe$_2$O$_4$/CNTs nanocomposite exhibited a stronger absorption band than the pristine MgFe$_2$O$_4$ NPs. The red shift in the absorption spectra of MgFe$_2$O$_4$/CNTs nanocomposite may be attributed to the interactions between MWCNTs and MgFe$_2$O$_4$ NPs. Because of the intense absorption in the visible region, the nanocomposite might have superb photocatalytic activity under visible-light irradiation. The optical band gap energy (Eg) of the samples was calculated based on Tauc's formula [52].

$$\alpha h \nu = A(h\nu - Eg)^2 \qquad (5)$$

where α, h, ν, Eg, and A denote the absorption coefficient, Planck constant, light frequency, optical band gap energy and a constant, respectively. As shown in Fig. 7 (right), the tangent line intercepts with $h\nu$ axis were extrapolated to get Eg values of 1.99 and 1.87 eV, for

MgFe$_2$O$_4$ NPs and MgFe$_2$O$_4$/CNTs nanocomposite, respectively. The reduction in the band gap value of MgFe$_2$O$_4$/CNTs nanocomposite may be attributed to the successful formation of an active heterojunction between the MgFe$_2$O$_4$ NPs and MWCNTs from one side, and the strongly electron-conducting MWCNTs from the other. These results, however, agree with the results obtained from the interaction between CNTs@SiC nanocomposite [53]. In conclusion, the smaller band gap energy leads to a higher absorption efficiency under visible light, resulting in the formation of more electron-hole pairs during photolysis reactions.

Fig. 7. **(left):** UV-visible diffuse reflectance spectra of MgFe$_2$O$_4$ and MgFe$_2$O$_4$/CNTs; **(right):** Determination of the optical band gap energies of MgFe$_2$O$_4$ and MgFe$_2$O$_4$/CNTs nanocomposite.

- -

3.5. Photocatalytic activity by UV-visible spectroscopy

The catalytic efficiency of our MgFe$_2$O$_4$/CNTs nanocomposite catalyst was studied through utilizing the photodegradation reaction of methylene blue (MB) in aqueous solution under solar radiation. The photocatalytic efficiency of MgFe$_2$O$_4$ NPs was also studied for comparison purposes. Irradiation of MB for 25 min without catalyst was also examined and it was found that the MB was sunlight-stable. The UV-vis spectra (Fig. 8a) revealed that our synthesized MgFe$_2$O$_4$/CNTs nanocomposite possessed excellent photocatalytic activity under sunlight. Our synthesized MgFe$_2$O$_4$/CNTs nanocomposite catalyst exhibited superior absorption ability, with a photodegradation yield reaching 98% after 25 min, while that of pristine MgFe$_2$O$_4$ NPs was only 25.5% for the same irradiation time (Fig. 8b). Although pristine MgFe$_2$O$_4$ NPs has a narrow band gap (1.99 eV), it showed less capability to utilize sunlight effectively; this may be due to its smaller surface area (4.626 m^2 g^{-1}) or partly perhaps to a higher overpotential for photo-oxidation on the MgFe$_2$O$_4$ surface. The fast backward recombination between electrons in the conduction band (CB) and holes in the valence band (VB) in pristine MgFe$_2$O$_4$ NPs makes it less active as a photocatalyst compared with MgFe$_2$O$_4$ /CNTs [54].

Fig. 8. Photocatalytic performance evaluations: (a) absorption spectra of the MB (10 mg.L^{-1}) solution at different photocatalytic times using MgFe$_2$O$_4$/CNTs photocatalyst (b) photocatalytic degradation of MB and (c) reaction kinetics curves of MB with the MgFe$_2$O$_4$/CNTs nanocomposite.

(a)

(b)

(c)

$k=0.15621 \ min^{-1}$

$k=0.01122 \ min^{-1}$
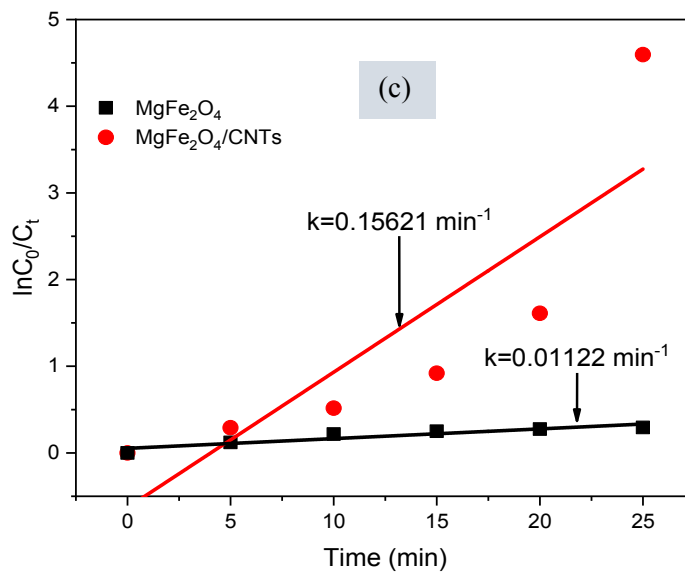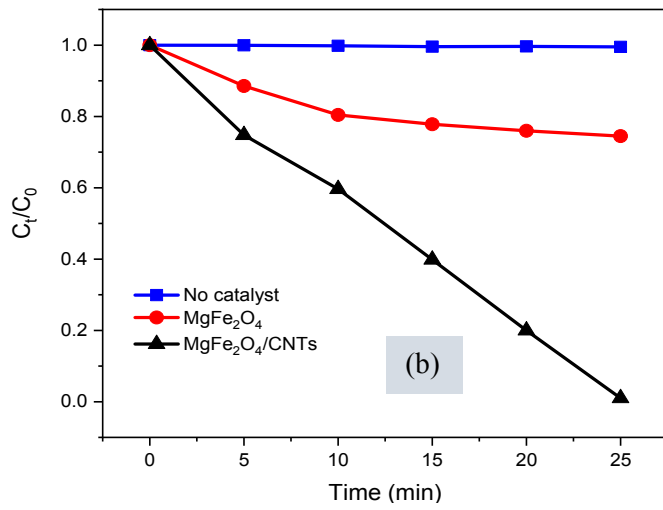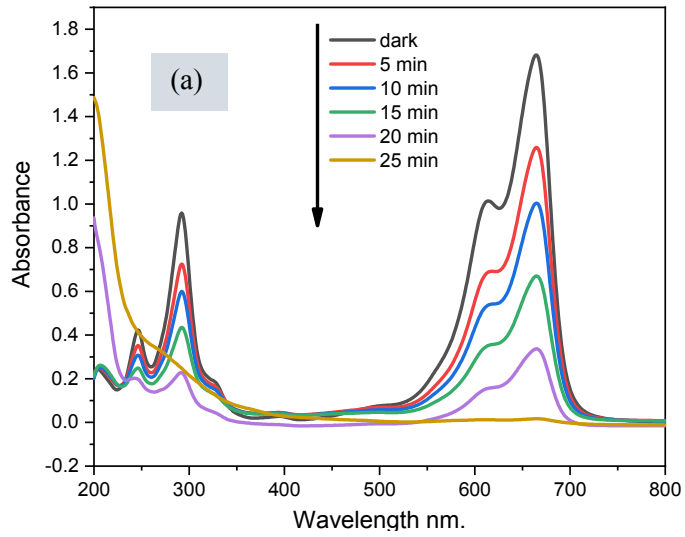
The photodegradation activity of MB in an aqueous suspension solution containing either pristine $MgFe_2O_4$ nanoparticles or $MgFe_2O_4$/CNTs nanocomposite catalyst under sunlight was found to follow the pseudo-first-order kinetic model:

$$dC/dt = k\,C \qquad (6)$$

where k is the apparent reaction rate constant $[min^{-1}]$. Integrating of equation (6) yields the following relation:

$$\ln C_0/C_t = k\,t \qquad (7)$$

Based on equation (7), a plot of $\ln(C_0/C_t)$ vs. irradiation time yields a slope of k. The graphical results are shown in Fig. 8c. The value of the rate constant k of $MgFe_2O_4$/CNTs nanocomposite was calculated to be $0.15621\ min^{-1}$, which is higher than that for pristine $MgFe_2O_4$ NPs ($k = 0.01122\ min^{-1}$). It is clear that the synergistic effect between $MgFe_2O_4$ and MWCNTs plays a vital role in enhancing the photocatalytic activity of our MFO/CNTs nano-catalyst. However, the high photoactivity of the $MgFe_2O_4$/CNTs nanocomposite may be interpreted by considering the following: the large surface area of $MgFe_2O_4$/CNTs provided more accessible active sites for photodegradation reaction of MB; and the efficient charge separation of photogenerated electron-hole pairs by much more direct pathways for electron transport to suppress the charge recombination [55]. Another factor which may be considered is the ease of MB molecular adsorption onto the photocatalyst surface via π-π conjugation between the MB molecule and the aromatic frames of MWCNTs [56].

To examine the main active species responsible for MB photodegradation reaction and to understand the reaction mechanism thoroughly, the ESR-DMPO technique was used to confirm the reactive oxygen species (ROS) produced by $MgFe_2O_4$/CNTs nanocomposite during the photocatalytic process. The results were interpreted by a similar scenario to that proposed for the $CaFe_2O_4$/g-C_3N_4/CNT system [57]. As shown in Fig. 9a and b, $MgFe_2O_4$/CNTs nanocomposite showed no ESR signal corresponding to DMPO-$^{\bullet}O_2^{-}$ and DMPO-$^{\bullet}OH$ radicals in the dark. Upon irradiation with solar energy for progressive time intervals, our photocatalyst i.e. $MgFe_2O_4$/CNTs clearly indicated ESR signals related to DMPO-$^{\bullet}O_2^{-}$ and DMPO-$^{\bullet}OH$ which are associated with $^{\bullet}O_2^{-}$ and $^{\bullet}OH$ radicals. These reactive species i.e. $^{\bullet}O_2^{-}$ and $^{\bullet}OH$ in their turn initiate the photodegradation reaction of MB in the catalytic system. Moreover, the evident increase in the ESR signals intensity with increasing irradiation time supports the existence of the photoexcited charge carriers (electron-hole pairs) separation which decreases the probability of recombination. Furthermore, the higher intensities of the characteristic ESR peaks of DMPO-$^{\bullet}O_2^{-}$ confirm that the superior catalytic performance of $MgFe_2O_4$/CNTs nanocomposite as photocatalyst is attributable mainly to

superoxide radicals ($O^{\bullet-}$). Although the ESR signals for the DMPO-$^{\bullet}$OH radicals were weaker than those of the DMPO-$^{\bullet}O_2^-$, this would not prevent the $^{\bullet}$OH radicals (or their H2O2 by-product) from destroying organic pollutants in wastewater, due to their relatively high oxidation capacity.

Depending on the above mentioned results, a reasonable mechanism is proposed to clarify the photocatalytic activity of the $MgFe_2O_4$/CNTs nanocomposite. To explain the efficient electron-hole separation in the $MgFe_2O_4$/CNTs nanocomposite, it is important to find the conduction band (CB) and valence band (VB) edge positions of the $MgFe_2O_4$. The potentials of the VB and CB were calculated using the following empirical formulas [58]:

$$E_{CB} = X - E^e - 0.5E_g \qquad \textbf{(8)}$$

$$E_{VB} = E_{CB} + E_g \qquad \textbf{(9)}$$

where E_{VB} and E_{CB} stand for VB and CB potentials, respectively, E^e is the energy of free electrons vs. hydrogen scale (4.5 eV), and X is the electronegativity of the semiconductor compound, which is calculated using the following formula:

$$X = [x(A)^a x(B)^b x(C)^c]^{\frac{1}{a+b+c}} \qquad \textbf{(10)}$$

where a, b, and c are the number of atoms in the semiconductor compounds. According to the above formulas, the (CB) and (VB) potentials of $MgFe_2O_4$ were calculated to be 0.175 and 2.165 eV/NHE, respectively. According to the above results and band gap structures of $MgFe_2O_4$, the suggested mechanism by which $MgFe_2O_4$/CNTs nanocomposite acts on MB photodegradation under sunlight irradiation is presented in Fig. 9c. Under sunlight irradiation, the electrons (e$^-$) are excited from the VB to CB of $MgFe_2O_4$ leaving a hole (h$^+$) in the VB and generating an electron-hole pairs. Although $MgFe_2O_4$ has a band gap of 1.99eV, electrons on the CB of $MgFe_2O_4$ were unable to reduce O_2 to form $^{\bullet}O_2^-$ radicals because the CB edge position of $MgFe_2O_4$ was more positive than the potential of $O_2/^{\bullet}O_2^-$ (−0.33 eV vs. NHE) [59]. On the other hand, the holes of $MgFe_2O_4$ can oxidize OH$^-$ to give $^{\bullet}$OH because the VB potential of OH$^-$ is higher than the redox potential of OH$^-/^{\bullet}$OH (1.89 eV vs. NHE) [60]. Upon anchoring $MgFe_2O_4$ nanoparticles on the MWCNTs, electron transfer from the CB of the photo-excited $MgFe_2O_4$ to the MWCNTs, allows the formation of interfacial barriers between the $MgFe_2O_4$ and MWCNTs. These, in turn, provide efficient separation of the photoexcited charge carriers, resulting in the suppression of the recombination of photoexcited electron-hole pairs. The excited electrons can be shuttled freely along the

conducting network of MWCNTs and subsequently transfer to the surface to react with oxygen-releasing superoxide ($^{\bullet}O_2^{-}$) which acts as an MB oxidizer [61]. Simultaneously, the generated holes in (VB) of $MgFe_2O_4$ incorporated with MWCNTs produce hydroxyl radicals ($^{\bullet}OH$) via the reaction of hole charge (h^+) with OH^- which acts as MB oxidizer as well. Hence, the photocatalytic performance of $MgFe_2O_4$/CNTs nanocomposite was enhanced dramatically. The detailed reaction steps of the mechanism are described below, similarly to a scheme reported in the literature [62].

$$MgFe_2O_4 \qquad\qquad MgFe_2O_4(h^+_{VB} + e^-_{CB}) \qquad\qquad (11)$$

$$MgFe_2O_4(e^-) + MWCNTs \qquad\qquad MgFe_2O_4 + MWCNTs(e^-) \qquad (12)$$

$$MWCNTs(e^-) + O_2 \qquad\qquad MWCNTs + O_2^{\bullet-} \qquad\qquad (13)$$

$$O_2^{\bullet-} + H_2O \longrightarrow HO_2^{\bullet} + {}^-OH \qquad\qquad (14)$$

$$HO_2^{\bullet} + H_2O \longrightarrow HO^{\bullet} + H_2O_2 \qquad\qquad (15)$$

$$H_2O_2 \longrightarrow 2HO^{\bullet} \qquad\qquad (16)$$

$$MgFe_2O_4(h^+) + {}^-OH \longrightarrow MgFe_2O_4(h^+) + HO^{\bullet} \qquad (17)$$

$$MB + HO^{\bullet} \text{ or } O_2^{\bullet-} \longrightarrow H_2O + CO_2 + SO_4^{2-} + \text{other small molecules} \qquad (18)$$
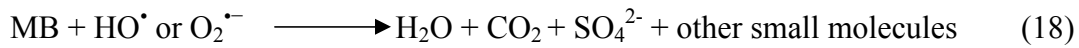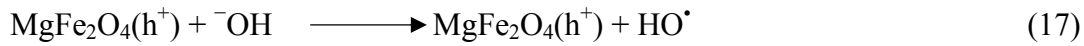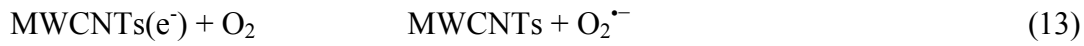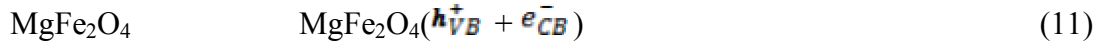
Fig. 9. ESR spectra of $MgFe_2O_4$/CNTs nanocomposite (a) in methanol dispersion (for DMPO-$^{\bullet}O_2^{-}$) (b) and in aqueous dispersion (for DMPO-$^{\bullet}OH$) under simulated solar irradiation. (c) Schematic diagram of proposed mechanism for enhanced degradation of MB by $MgFe_2O_4$/CNTs heterojunction photocatalyst under sunlight irradiation.

(a)
(b)

(c)

3.6 Optimizing Photocatalytic performance

To optimize the photocatalytic degradation efficiency of our nanocatalyst, parameters such as catalyst dose, pH at which photodegradation of MB occurred and MB concentration were investigated. Different pH values (pH=2–12) were used to determine the optimum value for

degradation efficiency. The influence of pH on the degradation efficiency of MB dye over MgFe$_2$O$_4$/CNTs can be seen in Fig. 10a. The graphical data shows that under acidic conditions (pH=2~4), our nanocatalyst exhibited poor photocatalytic efficiency, while under mild alkaline conditions i.e. (pH=6~8), MB dye degradation efficiency increased significantly. These results can be explained as follows: it is well-known that many photocatalysts have amphoteric characteristics, including most metal oxides [63]. The formation of metal hydroxyl groups (M-OH) is attributed to the adsorption of H$_2$O molecules and dissociation of OH$^-$ groups at surface metal positions. The equilibrium of amphoteric metal hydroxides under acidic and alkaline conditions can be illustrated as follows:

$$M\text{-}OH + H^+ \longrightarrow M\text{-}OH\text{-}H^+ \longrightarrow M\text{-}H_2O^+ \qquad (19)$$

$$M\text{-}OH + OH^- \longrightarrow M\text{-}O^- + H_2O \qquad (20)$$
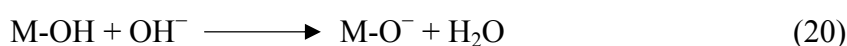
Therefore, in the acidic medium, the protonation of the photocatalyst forms a positively charged surface, which makes the photocatalyst behave as a strong Lewis acid versus a strong Lewis base which is an anionic dye. So, the positively charged surfaces of the catalyst tended to oppose the adsorption of cationic adsorbate species (cationic dyes). On the other hand, cationic dyes prefer to adsorb onto the negatively-charged surfaces in alkaline media, due to the high electrostatic attraction there. This explanation is in agreement with literature accounts published elsewhere [64,65]. Our results were consistent with the above explanation, since the charge of the MFO/CNTs catalyst surface was negative in the alkaline media, thus enhancing the adsorption capacity of the MB dye.

Fig. 10. Effect of **(a)** solution pH on MB degradation (T=25°C, dye concentration= 10 mgL^{-1}, catalyst dose: 0.03 g, and 25 min contact time), **(b)** catalyst dose (g/L) (T=25°C, dye concentration= 10 mgL^{-1}, pH= 6, and 25 min contact time), and **(c)** MB concentration (mg/L) (T=25°C catalyst dose: 0.03 g, pH= 6, and 25 min contact time).
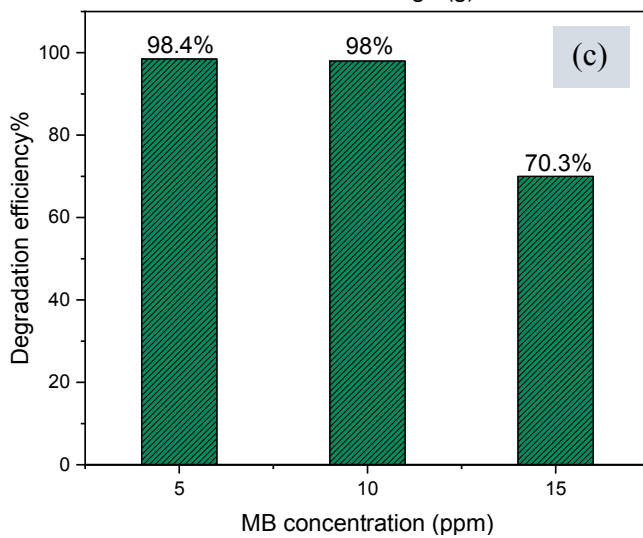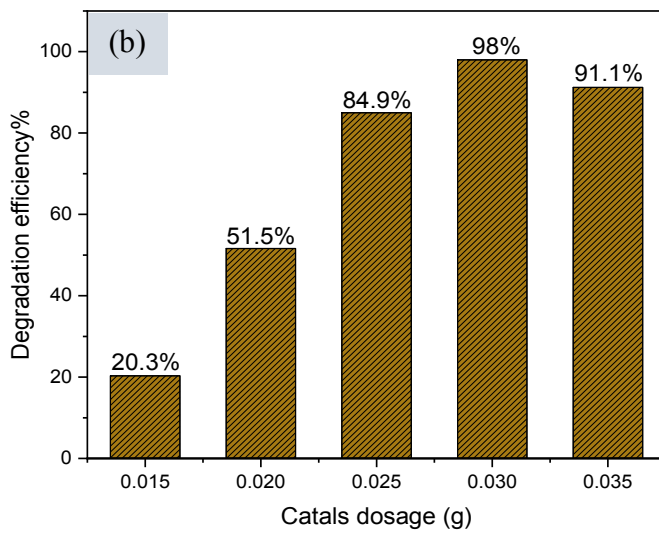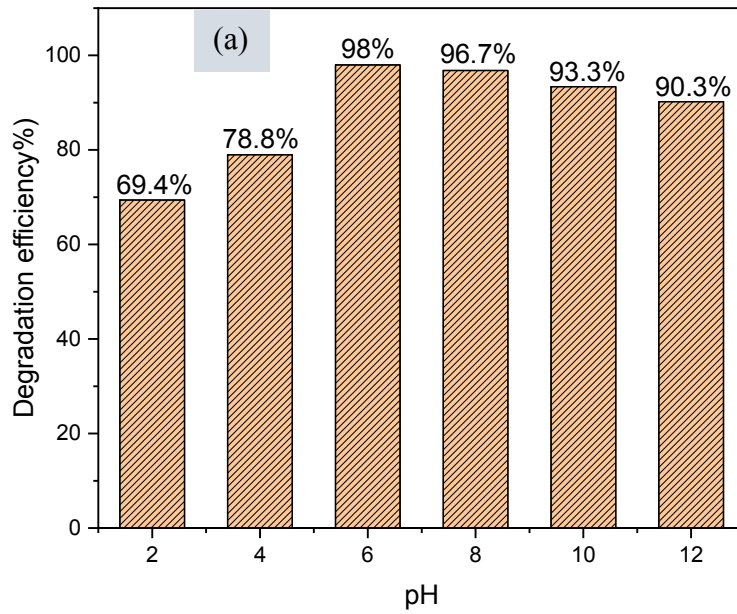
The effect of using different doses of MgFe$_2$O$_4$/CNTs nanocatalyst on photodegradation of MB is illustrated in Fig. 10b. It is apparent that 0.03 g/L MgFe$_2$O$_4$/CNTs nanocatalyst is the

optimum concentration for photocatalytic degradation of about 98% of MB after 25 min. Higher catalyst dosage increases the absorbed photons by the catalyst surface, hence increasing the generated electron-hole concentration and the number of adsorbed radicals. Nonetheless, a dosage of 0.035 g/L was found to slightly increase agglomeration of photocatalyst particles and hence reduce the penetration of photons into the active sites that the electron diffraction reveals [66]. Moreover, in order to investigate the effect of MB concentration on the photocatalytic performance, other MB concentrations i.e. 5, 10 and 15 ppm were used with an optimal $MgFe_2O_4$/CNTs nanocatalyst dosage of 0.03 g/L at pH=6 and 25 min irradiation time. The result in Fig. 10c shows that on increasing MB dye concentration from 5 to 15 ppm, a decline in degradation efficiency from 98.4 to 70.3 % can be observed. Higher MB concentration, however, can cause light scattering and fewer photons reach the particle surface. Hence, fewer electron-hole pairs are formed, i.e. low photodegradation efficiency.

Conclusion

$MgFe_2O_4$/CNTs nanocomposite photocatalyst has been successfully synthesized by PVA sol-gel microwave-assisted route. The CNTs appear to act as an efficient charge transfer medium to prevent the recombination of charges. The good photochemical properties and magnetic recyclability of $MgFe_2O_4$/CNTs make it a promising photocatalyst for efficient conversion of solar to chemical energy. The oxygen-containing functional groups (O-H, C=O, and C-O) on the surface of CNTs enhance the physical interaction between $MgFe_2O_4$ and MWCNTs. The partial coating of MWCNTs by $MgFe_2O_4$ nanoparticles increases access to the catalytic sites and thus leads to an increase in photocatalytic activity. The adsorption-desorption isotherms exhibited type IV isotherm H_3 hysteresis loops, which mainly indicate that the materials have mesoporous structure. The preparation methodology of our nanocatalyst enabled mesoporosity and high BET specific surface area (SA_{BET}) (40.051 m^2g^{-1}). The soft superparamagnetic behavior of $MgFe_2O_4$/CNTs enhances its recovery from water after being exposed to an external magnetic field. Under optimal conditions, our synthesized $MgFe_2O_4$/CNTs nanocomposite catalyst exhibited superior adsorption and catalytic ability, with a photodegradation yield reaching 98% after 25 min.

Acknowledgments

ORCID iD

Ibrahim F. Waheed https://orcid.org/0000-0002-8984-1783

Omer Yasin Thayee Al-Janabi https://orcid.org/0000-0001-5435-112X

Peter J. S. Foot https://orcid.org/0000-0002-2122-3129

Muayad A.S. Alkarawi https://orcid.org/0000-0002-0880-7883

References

[1]. Qian W, Wu Z, Jia Y, Hong Y, Xu X, You H, Zheng Y and Xia Y (2017) Thermo electrochemical coupling for room temperature thermocatalysis in pyroelectric ZnO nanorods. Electrochem Commun 81:124-127.

[2]. Ma J, Chen L, Wu Z, Chen J, Jia Y and Hu Y (2019) Pyroelectric $Pb(Zr_{0.52}Ti_{0.48})O_3$ polarized ceramic with strong pyro-driven catalysis for dye wastewater decomposition. Ceram Int 45:11934-11938.

[3]. Wang L, Haugen NO, Wu Z, Shu X, Jia Y, Ma J, Yu S, Li H and Chai Q (2019) Ferroelectric $BaTiO_3$@ZnO heterostructure nanofibers with enhanced pyroelectrically driven-catalysis. Ceram Int 45:90-95.

[4]. Djilani C, Zaghdoudi R, Djazi F et al (2015) Adsorption of dyes on activated carbon prepared from apricot stones and commercial activated carbon. J Taiwan Inst Chem E 53:112-121.

[5]. Ouaddari H, Karim A, Achiou B et al (2019) New low-cost ultrafiltration membrane made from purified natural clays for direct Red 80 dye removal. J Environ Chem Eng 7:103268.

[6]. Lan S, Feng J, Xiong Y, Tian S, Liu S and Kong L (2017) Performance and mechanism of piezo-catalytic degradation of 4-chlorophenol: Finding of effective piezo-dechlorination. Environ Sci Technol 51:6560-6569.

[7]. Xu X, Xiao L, Jia Y, Hong Y, Ma J and Wu Z (2018) Strong visible light photocatalytic activity of magnetically recyclable sol–gel-synthesized $ZnFe_2O_4$ for Rhodamine B degradation. J Electron Matter 47:536-541.

[8]. Raizada P, Sudhaik A and Singh P (2019) Photocatalytic water decontamination using graphene and ZnO coupled photocatalysts: a review. Mater Sci Energy Technol 2:509-525.

[9]. Ali IH and Alrafai HA (2016) Kinetic, isotherm and thermodynamic studies on biosorption of chromium(VI) by using activated carbon from leaves of Ficus nitida. Chem Cent J 10:36.

[10]. Jia J, Du X, Zhang Q, Liu E and Fan J (2019) Z-scheme $MgFe_2O_4/Bi_2MoO_6$ heterojunction photocatalyst with enhanced visible light photocatalytic activity for malachite green removal. Appl Surf Sci 492:527–539.

[11]. Byrne C, Subramanian G and Pillai SC (2018) Recent advances in photocatalysis for environmental applications. J Environ Chem Eng 6:3531-3555.

[12]. Shanthi M and Kuzhalosai V (2012) Photocatalytic degradation of an azo dye, acid red 27, in aqueous solution using nano ZnO. Indian J Chem 51A :428-434.

[13]. Xu X, Chen S, Wu Z, Jia Y, Xiao L and Liu Y (2018) Strong pyro-electro-chemical coupling of $Ba_{0.7}Sr_{0.3}TiO_3$@Ag pyroelectric nanoparticles for room-temperature pyrocatalysis. Nano Energy 50:581-588.

[14]. He C, Shu D, Su MH et al (2010) Photocatalytic activity of metal (Pt, Ag, and Cu)-deposited TiO_2 photoelectrodes for degradation of organic pollutants in aqueous solution. Desalination 253:88-93.

[15]. Ibrahim I, Athanasekou C, Manolis G et al (2019) Photocatalysis as an advanced reduction process (ARP): The reduction of 4-nitrophenol using titania nanotubes-ferrite nanocomposites. J Hazard Mater 372:37-44.

[16]. Manohar A and Krishnamoorth C (2017) Photocatalytic study and superparamagnetic nature of Zn-doped $MgFe_2O_4$ colloidal size nanocrystals prepared by solvothermal reflux method. J Photochem and Photobio B: Biol, 173:456-465.

[17]. Sonu V, Dutta S, Sharma P et al (2019) Review on augmentation in photocatalytic activity of $CoFe_2O_4$ via heterojunction formation for photocatalysis of organic pollutants in water. J Saudi Chem Soc. https://doi.org/10.1016/j.jscs.2019.07.003

[18]. Tzvetkov M, Milanova M, Cherkezova-Zheleva Z et al (2017) Mixed Metal Oxides of the Type $Co_xZn_{1-x}Fe_2O_4$ as Photocatalysts for Malachite Green Degradation Under UV Light Irradiation. Acta Chimica Slov 64:299-311.

[19]. Arimi A, Megatif L, Granone LI et al (2018) Visible-light photocatalytic activity of zinc ferrites. J Photochem Photobio A: Chem 366:118-126.

[20]. Rashmi SK, Naik HSB, Jayadevappa H et al (2017) Solar light responsive Sm-Zn

ferrite nanoparticle as efficient photocatalyst. Mater Sci Eng: B 225:86-97.

[21]. Gore SK, Jadhav SS, Jadhav S et al (2017) The structural and magnetic properties of dual phase cobalt ferrite. Scient rep 7:2524.

[22]. Babu KV, Sailaja B, Jalaiah K, Shibeshi PT and Ravi M (2018) Effect of zinc substitution on the structural, electrical and magnetic properties of nano-structured $Ni_{0.5}Co_{0.5}Fe_2O_4$ ferrites. Physica B: Condens Matter 534:83-89.

[23]. Sharma S, Choudhary N, Verma MK et al (2017) Cation distribution and magnetic properties of nano and bulk $CoCrFeO_4$ ferrite synthesized by glycine-nitrate combustion method. Ceram Int 43:11083-11089.

[24]. Reddy CVG, Manorama SV and Rao VJ (1999) Semiconducting gas sensor for chlorine based on inverse spinel nickel ferrite. Sen Actuators B 55:90-95.

[25]. Ahmed MA, Okasha N and El-Sayed MM (2007) Enhancement of the physical properties of rare-earth-substituted Mn–Zn ferrites prepared by flash method. Ceram Int 33:49-58.

[26]. Godbole RV, Rao P, Alegaonkar PS and Bhagwat S (2015) Influence of fuel to oxidizer ratio on LPG sensing performance of $MgFe_2O_4$ nanoparticles. Mater Chem Phys 161:1-7.

[27]. Feng Y, Li S, Zheng Y, Yi Z, He Y and Yebin Xu (2017) Preparation and characterization of $MgFe_2O_4$ nanocrystallites via PVA sol-gel route. J Alloys Compd 699:521-525.

[28]. Jinhui J, Kuili L, Weiqiang F et al (2016) Electrospinning synthesis and photocatalytic property of $Fe_2O_3/MgFe_2O_4$ heterostructure for photocatalytic degradation of tetracycline. Mater Lett 176:1-4.

[29]. Shahid M, Jingling L, Ali Z et al (2013) Photocatalytic degradation of methylene blue on magnetically separable $MgFe_2O_4$ under visible light irradiation. Mater. Chem. Phys 139:566-571.

[30]. Shakir I, Sarfraz M, Ali Z, Aboud MF and Agboola PO (2016) Magnetically separable and recyclable graphene-$MgFe_2O_4$ nanocomposites for enhanced photocatalytic applications. J Alloys Compd 660:450-455.

[31]. Skliri E, Miao J, Xie J et al (2018) Assembly and photochemical properties of mesoporous networks of spinel ferrite nanoparticles for environmental photocatalytic remediation. Appl Catal B: Environ 227:330-339.

[32]. Hong Y, Ren A, Jiang Y, He J, Xiao L and Shi W (2015) Sol–gel synthesis of visible-light-driven $Ni_{1-x}Cu_xFe_2O_4$ photocatalysts for degradation of tetracycline.

Ceram Int 41:1477-1486.

[33]. Zhang L, He Y, Wu Y and Wua T (2011) Photocatalytic degradation of RhB over MgFe$_2$O$_4$/TiO$_2$ composite materials. Mat Sci Eng: B 176:1497-1504.

[34]. Kaur N and Kaur M (2018) Envisioning the composition effect on structural, magnetic, thermal and optical properties of mesoporous MgFe$_2$O$_4$-GO nanocomposites. Ceram Int 44:4158-4168.

[35]. Li X, Lu H, Zhang Y and He F (2017) Efficient removal of organic pollutants from aqueous media using newly synthesized polypyrrole/CNTs-CoFe$_2$O$_4$ magnetic nanocomposites. Chem Eng J 316:893-902.

[36]. Zhu HY, Jiang R, Huang SH et al (2015) Novel magnetic NiFe$_2$O$_4$/multi-walled carbon nanotubes hybrids: Facile synthesis, characterization, and application to the treatment of dyeing wastewater. Ceram Int 41:11625-11631.

[37]. Cong Y, Li X, Qin Y et al (2011) Carbon-doped TiO$_2$ coating on multiwalled carbon nanotubes with higher visible light photocatalytic activity. Appl Catal B 107:128-134.

[38]. Singh C, Bansal S and Singhal S (2014) Synthesis of Zn$_{1-x}$Co$_x$Fe$_2$O$_4$/MWCNTs nanocomposites using reverse micelle method: Investigation of their structural, magnetic, electrical, optical and photocatalytic properties. Physica B: Condens Matter 444:70-76.

[39]. Shaheen HA, Marwani HM and Soliman EM (2015) Selective adsorption of gold ions from complex system using oxidized multi-walled carbon nanotubes. J Mol Liq 212:480-486.

[40]. Peddis D, Cannas C, Musinu A et al (2013) Beyond the effect of particle size: Influence of CoFe$_2$O$_4$ nanoparticle arrangements on magnetic properties. Chem Mater 25:2005-2013.

[41]. Yadav RS, Kuřitka I, Vilcakova J et al (2017) Impact of grain size and structural changes on magnetic, dielectric, electrical, impedance and modulus spectroscopic characteristics of CoFe$_2$O$_4$ nanoparticles synthesized by honey mediated sol-gel combustion method. Adv Nat Sci: Nanosci Nanotech 8:1-14.

[42]. Jianfeng WU, Meng LIU, Binzheng F, Fengyi Z, Na Z and Xiaohong XU (2009) Process control of zinc oxide nano crystalline prepared by a polyacylamide-gel method. J Chin Silic Soc 37:1782-1790.

[43]. Hu X, Liu B, Deng Y, Chen H, Luo S, Sun C and Yang S (2011) Adsorption and heterogeneous Fenton degradation of 17α-methyltestosterone on nano Fe$_3$O$_4$/MWCNTs in aqueous solution. Appl Catal B Environ.107:274-283.

[44]. Heiba ZK, Sanad MMS and Mohamed MB (2019) Influence of Mg-deficiency on the functional properties of magnesium ferrite anode material. Solid State Ionics 341:115042.

[45]. Abega AV, Ngomo HM, Nongwe I et al (2019) Easy and convenient synthesis of CNT/TiO$_2$ nanohybrid by in-surface oxidation of Ti^{3+} ions and application in the photocatalytic degradation of organic contaminants in water. Synth Met 251:1-14

[46]. Zhang X, Feng M, Wang L, Qu R and Wang Z (2017) Catalytic degradation of 2-phenylbenzimidazole-5-sulfonic acid by peroxymonosulfate activated with nitrogen and sulfur co-doped CNTs-COOH loaded CuFe$_2$O$_4$. Chem Eng J 307:95-104.

[47]. Jaafarzadeh N, Ghanbari F, Ahmadi M (2017) Efficient degradation of 2,4-dichlorophenoxyacetic acid by peroxymonosulfate/magnetic copper ferrite nanoparticles/ozone: A novel combination of advanced oxidation processes. Chem Eng J 320:436-447.

[48]. Shi D, Cheng JP, Liu F and Zhang XB (2010) Controlling the size and size distribution of magnetite nanoparticles on carbon nanotubes. J Alloys Compd 502:365-370.

[49]. Kafshgari LA, Ghorbani M and Azizi A (2017) Fabrication and investigation of MnFe$_2$O$_4$/MWCNTs nanocomposite by hydrothermal technique and adsorption of cationic and anionic dyes. Appl Surf Sci 419:70-83.

[50]. Ain N, Shaheen W, Bashir B, Abdelsalam NM, Warsi MF, Khan MA and Shahid M (2016) Electrical, magnetic and photoelectrochemical activity of rGO/MgFe$_2$O$_4$ nanocomposites under visible light irradiation. Ceram Int. 42:12401-12408.

[51]. Cullity BD and Chad DG (2011) Introduction to magnetic materials. John Wiley & Sons. USA.

[52]. Zhu Z, Wang C, Liang L, Yu D, Sun J, Zhang L, Zhong S and Liu B (2020) Synthesis of novel ternary photocatalyst Ag$_3$PO$_4$/Bi$_2$WO$_6$/Multi-Walled Carbon nanotubes and its enhanced visible-light photoactivity for photodegradation of norfloxacin. J Nanosci Nanotechnol 20:2247-2258.

[53]. Zhou X, Gao Q, Yang S and Fang Y (2020) Carbon nanotube@silicon carbide coaxial heterojunction nanotubes as metal-free photocatalysts for enhanced hydrogen evolution. Chinese Journal of Catalysis 41: 62-71.

[54]. Wu F, Duan W, Li M and Xu H (2018) Synthesis of MgFe$_2$O$_4$/reduced graphene oxide composite and Its visible-light photocatalytic performance for organic pollution. Int J Photoenergy 2018:1-5.

[55]. Sohail M, Xue H, Jiao Q et al (2018) Synthesis of well-dispersed $TiO_2/CNTs@CoFe_2O_4$ nanocomposites and their photocatalytic properties. Mater Res Bulletin 101:83-89.

[56]. Zhao D, Yang X, Chen C and Wang X (2013) Enhanced photocatalytic degradation of methylene blue on multiwalled carbon nanotubes-TiO_2. J Colloid Interface Sci 398:234-239.

[57]. Liu F, Dong S, Zhang Z, Li X, Dai X, Xin Y, Wang X, Liu K, Yuan Z and Zheng Z (2019) Synthesis of a well-dispersed $CaFe_2O_4/g$-C_3N_4/CNT composite towards the degradation of toxic water pollutants under visible light. RSC Adv 9:25750-25761.

[58]. Jiang L, Yuan X, Zeng G, Liang J, Chen X, Yu H, Wang H, Wu Z, Zhang J and Xiong T (2018) In-situ synthesis of direct solid-state dual Z-scheme WO_3/g-C_3N_4/Bi_2O_3 photocatalyst for the degradation of refractory pollutant. Appl Catal B: Environ 227:376-385.

[59]. Wang J, Tang L, Zeng G, Liu Y, Zhou Y, Deng Y, Wang J and Peng B (2017) Plasmonic bi metal deposition and g-C_3N_4 coating on Bi_2WO_6 microspheres for efficient visible-light photocatalysis. ACS Sustain Chem Eng 5:1062-1072.

[60]. Tachikawa T, Fujitsuka M and Majima T (2007) Mechanistic insight into the TiO_2 photocatalytic reactions: design of new photocatalysts. J Phys Chem C 111:5259-5275.

[61]. Askari MB, Banizi ZT, Soltani S and Seifi M (2018) Comparison of optical properties and photocatalytic behavior of $TiO_2/CdS/MWCNTs$ nanocomposites. Optik 157:230-239.

[62]. Lu M, Chang Y, Guan X-H and Wang G-S (2019) The synthesis of $Co_xNi_{1-x}Fe_2O_4$/multi-walled carbon nanotube nanocomposites and their photocatalytic performance. RSC Adv 9:33806-33813.

[63]. Chiu Y-H, Chang T-FM, Chen C-Y, Sone M and Hsu Y-J (2019) Mechanistic insights into photodegradation of organic dyes using heterostructure photocatalysts. Catalysts 9:1-32.

[64]. Devi LG and Kumar SG (2012) Exploring the critical dependence of adsorption of various dyes on the degradation rate using Ln^{3+}-TiO_2 surface under UV/solar light. Appl Surf Sci 261:137-146.

[65]. Zajac K, Choina J, Dolat D and Morawski A (2010) Methylene blue and phenol photocatalytic degradation on nanoparticles of anatase TiO_2. Pol J Environ Stud 19:685-691.

[66]. Sirajudheen P and Meenakshi S (2019) Facile synthesis of chitosan-La^{3+}-graphite composite and its influence in photocatalytic degradation of methylene blue. Int J Biol Macromol 133:253-261.